Composites Part C: Open Access 6 (2021) 100191

Contents lists available at ScienceDirect

Composites Part C: Open Access

journal homepage: www.elsevier.com/locate/composites-part-c-open-access

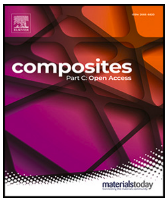

Strain sensing in GFRP via fully integrated carbon nanotube epoxy film sensors

Christina Buggisch [*], Dennis Gibhardt, Nils Felmet, Yannick Tetzner, Bodo Fiedler

Hamburg University of Technology, Institute of Polymers and Composites, Denickestraße 15, 21073 Hamburg, Germany

ARTICLE INFO

Keywords:
Glass fibre
Multifunctional composite
SHM
Health monitoring
Damage

ABSTRACT

Structural health monitoring of composite structures enables early damage detection to prevent critical component failure. Surface-mounted strain gauges are commonly applied to monitor the integrity of composite structures in highly loaded areas. However, strain gauges can only measure strain on the structure's surface and are exposed to environmental influences. Within this paper, fully integrated carbon nanotube thin-film sensors for strain and damage sensing in glass fibre reinforced polymers (GFRP) via electrical resistance measurements are presented. Single wall carbon nanotube epoxy thin-films were manufactured using a manual film applicator, partially pre-cured, placed on dry glass fabrics and infused in a resin transfer moulding process. The mechanical properties of the composites and strain sensing capabilities of the integrated sensors were studied for various load cases and different laminate lay-ups. Results of quasi-static and step-wise three-point bending and tensile tests show that the integrated films allow for localised strain measurements in GFRP without significant loss of mechanical properties. Open hole tensile tests proof the ability to monitor local strain and damage in highly loaded areas enabling failure prediction via threshold resistance change values. The proposed thin-films enable a tailored strain and damage monitoring of GFRP offering the possibility for measurements at different material depths, over large sections or selectively in highly loaded areas. The manufacturing process is easily automatable and suitable for large scale manufacturing.

1. Introduction

Monitoring of the integrity of fibre reinforced composite structures during operation can enable early damage detection, which significantly enhances the safety of the structures and reduces inspection costs and expensive machine downtimes. Many promising structural health monitoring (SHM) methods are part of ongoing research (fibre Bragg sensors, electrical measurements, acoustic emission, wave propagation) [1–3]. Despite all advanced SHM methods, local strain measurements of composite components using surface-mounted strain gauges in critical loading areas are still common as no expensive measuring equipment is required. However, surface-mounted strain gauges only monitor small areas, cannot provide information about internal strains and are susceptible to external influences. Furthermore, installation at many points requires long installation times and a complex wire routing. Self-sensing materials or embedded strain sensors that do not negatively influence the mechanical properties of fibre reinforced polymers (FRP) are therefore desirable. The material's intrinsic electrical conductivity in carbon fibre reinforced polymers (CFRP) can be used for strain measurement and damage detection [4,5]. Unfortunately, such intrinsic strain measurements are not possible in electrically non-conductive polymers, or glass fibre reinforced polymers (GFRP). Extensive research on carbon nanoparticles (carbon black, graphene and carbon nanotubes (CNTs)) lead to exploiting the sensing potential of electrically conductive polymer nanocomposites. By dispersing carbon nanoparticles in polymers, a conductive network is formed when the filler content is above the percolation threshold. This piezoresistive network is susceptible to applied mechanical loads as conductive paths are formed or dissolved with deformation. Carmona et al. [6] conducted an early study of the piezoresistive behaviour of nanocomposites with different carbon particle/polymer combinations by analysing the influence of hydrostatic pressure on resistivity. Many researchers have proved the strain sensing ability of carbon nanocomposites for different filler types and under various load cases as summarised in a review paper by Zhang et al. [7]. Advances regarding manufacturing, understanding and sensitivity of the piezoresistive nanoparticle/polymer sensors are still part of ongoing research [8,9]. Using modified polymers as matrix material of FRP enables the manufacturing of GFRP with conductive matrix and intrinsic strain and damage sensing properties. When first integrating carbon

---

[*] Corresponding author.
E-mail address: christina.buggisch@tuhh.de (C. Buggisch).

https://doi.org/10.1016/j.jcomc.2021.100191
Received 31 August 2021; Received in revised form 17 September 2021; Accepted 21 September 2021
Available online 28 September 2021

nanoparticles in FRP, the whole matrix material was modified with conductive carbon nanoparticles. Kupke et al. [10] manufactured a conductive GFRP by modification of the epoxy matrix of prepregs using carbon black. Different groups showed the strain and damage monitoring capability of FRP with fully modified matrix [11–14]. An alignment of the carbon nanoparticles in a fully modified matrix leads to improvements of the fracture toughness and damage-detection sensitivity [15]. Especially for large structures, however, fully modifying the matrix is expensive, and no localised strain monitoring is possible. Many promising results have been published about surface-mounted carbon nanotube/polymer sensors on different substrates [16–22]. Therefore, pre-manufactured thin-films or CNT buckypapers have been adhesively bonded to the surface or deposited directly on different substrates by layer-by-layer deposition or spray coating and tested under various load cases. Similar to classical metal strain gauges, the surface-mounted sensors or conductive coatings are susceptible to external influences and damage. Research on integrated local modification of GFRP for resistive strain monitoring via fibre coating, partial modification of the matrix or embedding of CNT fibres or CNT film strain gauges in GFRP is still limited. Alexopoulos et al. [23] suggested a process with direct placement of CNT fibres, manufactured in an elaborate coagulation process, on dry glass fibre fabrics, which were infused in a vacuum infusion process. The mechanical tensile properties of the samples with embedded CNT fibres were found to be equal to non-modified specimens. In tensile and flexural tests, the authors were able to correlate the electrical resistance change with the applied strain. A modification of the fibre interphase of glass fibres with CNTs by the doctor knife method [24,25] or direct chemical vapour deposition (CVD) [26] showed promising results for strain sensing ability. However, these methods require many manufacturing steps and are therefore hard to automate or realise on a large scale. Gao et al. [27] showed the possibility of strain, temperature and relative humidity sensing in GFRP via electrical resistance measurements when dipping entire dry glass fabrics in various aqueous MWCNT dispersions and infusing the dried fabrics with epoxy. More advanced methods for applying CNTs directly on dry glass fibre fabrics are layer-by-layer (LbL) deposition or spray coating [28–31]. The methods showed promising results regarding piezoresistive strain and damage sensing under different load cases. Spray application of CNTs requires many safety precautions. Another possibility to locally integrate CNTs in GFRP is by using CNT buckypapers or CNT sheets. Aly et al. [32,33] suggested a method to implement aligned CNT sheets in the interlaminar region of GFRP prepreg laminates and proofed the strain sensing capabilities under various forms of tensile [32] and flexural loading [33]. Kravchenko et al. [34,35] embedded CNT buckypapers in the large areas of the interlaminar region using frictional roller sliding on glass fabrics in a wet hand lay-up process. They found an increase in mode I and mode II interlaminar fracture toughness and a strain and damage monitoring capability through resistance measurements. The manufacturing process using wet hand lay-up is hard to automate and susceptible to manufacturing deviations. Especially on an industrial scale, GFRP parts as wind turbine rotor blades are manufactured in a vacuum infusion process. In a study by Wu et al. [36], a commercial buckypaper with randomly oriented CNTs manufactured in a CVD process was used as a conductive interlayer in GFRP composites. The buckypaper was placed directly on the dry glass fabric and then infused by vacuum infusion. During high strain rate compressive loading using a Hopkinson bar, the in-situ electrical resistance is measured, and the resistance increase provided information about strain and damage inside the specimen. CNT buckypapers require a high caution during handling as they can easily break. Slobodian [37] integrated entangled MWCNT buckypaper manufactured with vacuum filtration on a polyurethane membrane in GFRP laminates during vacuum infusion. They showed a resistance change during infusion as well as during bending over a cylindrical surface. When including the filter membranes, e.g. polyurethane, in the final composite, the influences on the connection with the used matrix polymer have to be considered.

Table 1
Process parameters of three roll mill during masterbatch manufacturing.

Step	Back gap	Front gap	Speed
1	120 μm	40 μm	300 min^{-1}
2	40 μm	13 μm	300 min^{-1}
3–7	13 μm	5 μm	300 min^{-1}

An automatable technique enabling reliable, easy, fast and safe large-scale production of fully integrated sensors to measure strain and damage in FRP without significant loss of mechanical properties is desired [21]. The novel method presented in this paper aims to provide a solution to this problem. Therefore, a simple and automatable manufacturing process for embedding partially pre-cured SWCNT/epoxy films for strain and damage monitoring in GFRP is shown. The films are manufactured with a simple doctor blade technique using a dispersion of CNTs and epoxy resin. As the same epoxy system is used during film manufacturing and vacuum infusion process of the laminates and no additional membranes are needed, a chemical crosslinking between the films and the surrounding epoxy resin is likely. The flexible thin-film sensors provide easy handling during placement on dry glass fibre fabrics even on complicated or curved shapes. The films can be placed over large areas or very localised, enabling tailored strain monitoring in highly loaded areas and between different layers. This study examines the mechanical influence of the integrated SWCNT/epoxy films and their strain and damage sensing abilities under various load cases for different laminate lay-ups offering a comprehensive understanding of their use as sensors.

2. Materials and methods

2.1. Manufacturing of CNT/epoxy films

At first, a masterbatch of 1 wt% OCSiAl Tuball™ carbon nanotubes and EPIKOTE™ Resin MGS™ RIMR 135 (Hexcel, Germany) was manufactured using an 80E Plus three-roll mill (EXAKT Advanced Technologies, Germany). The process parameters of the three-roll mill process are given in Table 1. A more detailed description of the process is given by Meeuw et al. [38,39]. To achieve the desired filler content of 0.5 wt% CNT in the films, the masterbatch was mixed with the required amounts of EPIKOTE™ Resin MGS™ RIMR 135 and EPIKURE™ Curing Agent MGS™ RIMH 137. The weight ratio of resin and curing agent was 100:30, as defined by the manufacturer. The materials were premixed using a wooden spatula and final mixing was performed at 3000 min^{-1} for 3 min using a speed mixer. Films were manufactured with a thickness of 6 mils (152.4 μm) using a manual square film applicator (BYK 5358) on a polished steel plate covered in Teflon foil. Suitable filler content and thickness of the films have been evaluated in pre-tests. Prior to integration in GFRP plates, the films were cured under lab conditions at room temperature for 48 h.

2.2. Manufacturing of GFRP plate and specimens

GFRP laminates were manufactured in a resin transfer moulding process. Laminates with unidirectional (UD) and cross-ply (CP) lay-ups (compare Table 2) were manufactured using Gurit UT E-250 unidirectional non-crimp glass fibre fabrics. For open hole tensile (OHT) tests, a quasi-isotropic lay-up (compare Table 2) was set up from bidiagonal ±45° glass fibre fabric B320E-H form HP-Textiles and unidirectional glass fibre fabric UVE 926 from Saertex. During stacking of the dry glass fibre fabrics, the pre-cured CNT films were placed in the desired locations (shown in Fig. 1). Before placing, the Teflon foil was removed, and the films were cut to the desired shapes. For bending tests, the films were placed over the lowest glass fabric, in the symmetry plane

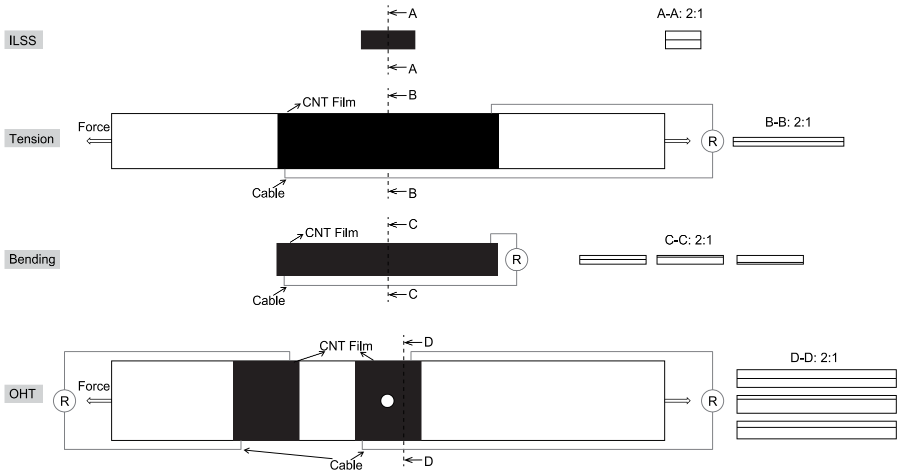

Fig. 1. Schematic representation of specimens (from top to bottom: ILSS, tensile, bending and OHT) including film and contacting positions.

Table 2
Layups, dimensions and film positions of GFRP specimens.

Test	Layup	Dimensions [LxWxT]	Film position
ILSS	UD: $[0_{16}]$	24 × 8 × 4 mm^3	Middle
Bending	UD: $[0_{10}]$ CP: $[0/90_4/0]_s$	100 × 15 × 2 mm^3	Middle, Under top ply Over bottom ply
Tensile	UD: $[0_{10}]$ CP: $[0/90_4]_s$	250 × 25 × 2 mm^3	Middle
OHT	QI: $[\pm 45_2/90/0]_s$	250 × 36 × 4 mm^3 Hole diameter: 6 mm	Between ±45° and 90° Between 90° and 0° Middle

Table 3
Force levels during force-controlled step-wise tests.

Tension		Bending	
UD	CP	UD	CP
5000 N	2600 N	40 N	40 N
10 000 N	3000 N	150 N	100 N
15 000 N	3400 N	250 N	150 N
25 000 N	4000 N	350 N	200 N
35 000 N	6800 N	450 N	250 N
		550 N	300 N

and directly under the upper fabric. In the ILSS and tensile specimens, the films were only placed in the symmetry plane. Three configurations of OHT film specimens were manufactured—including films between the ±45°-layer and the 90°-layer, between the 90°-layer and the 0°-layer and in the middle of the laminate between the 0°-plies. The two-component epoxy system EPIKOTE™ Resin MGS™ RIMR 135 and EPIKURE™ Curing Agent MGS™ RIMH 137 with a weight ratio of 100:30 was used for infusion. Curing was performed at 50 °C for 16 h and post-curing at 80 °C for 16 h. Specimens for ILSS, three-point bending, tensile and OHT tests were cut to the dimensions given in Table 2 using a Brillant 265 saw (ATM, Germany). The holes in the OHT specimen were milled using an Isel Euromod mill. All CNT films were contacted on the specimens' edges using Acheson 1415 conductive silver paint and LiFy cables with 0.25 mm^2 cross-section. Schematic representations of all specimens including contacting positions are shown in Fig. 1. The edges of some tensile specimens were painted with a speckle pattern with black paint splashes on white background for digital image correlation (DIC) measurements.

2.3. Test setup

The ILSS tests were performed according to ASTM D2344 [40] using a Z10 universal test machine (Zwick Roell, Germany). The diameter of the lower rollers was chosen as 3 mm, the diameter of the upper roller as 6 mm and the support distance as 16 mm. The test speed was 1 $\mathrm{mm\,min}^{-1}$. Additionally, quasi-static tests until final failure and force-controlled step-wise tests for tensile and bending loads were carried out on UD and CP specimens. Table 3 includes the force levels of the force-controlled step-wise tests. Furthermore, quasi-static OHT tensile tests until final failure were conducted. Three-point bending tests were performed using a Z10 universal test machine (Zwick Roell, Germany) following DIN EN ISO 14125 [41]. The upper roller diameter was set as 15 mm, the lower diameter as 10 mm and the support distance was 60 mm. Tensile and OHT tests were conducted at a test speed of 2 $\mathrm{mm\,min}^{-1}$ on a Z400 universal test machine (Zwick Roell, Germany). The tensile tests were performed according to DIN EN ISO 527-4 [42], and the strain was measured using a multiXtens contact extensometer. During some tensile tests, the local strain distribution was monitored on the specimens' edge using a GOM Aramis DIC system. For crack counting in CP tensile specimens, no speckle pattern was applied and only one camera of the DIC system was used for filming the specimens. The OHT tests were performed following ASTM D5766 [43]. During all tests of specimens including CNT films, the in-situ electrical resistance was measured. The resistance measurements on bending and tensile specimens were performed using a Keithley 2601 A. A constant voltage of 1 V was applied and the current was measured. In OHT tests, the resistance change was similarly evaluated using a two-channel Keithley 2602 for simultaneous measurements of two films included in the same specimen. One film was placed directly around the hole, and the other film was integrated in the near field—close to the clamping area furthest away from the hole.

3. Results and discussion

3.1. Micrographs

Fig. 2 shows micrographs of undamaged UD and CP specimens with films in the middle of the laminate and over the lower ply, which corresponds to those under the upper ply. Micrographs for two cutting directions are depicted for each configuration—parallel and transverse to the 0°-fibres. Over all configurations, the films in specimens cut parallel to the fibre direction of the upper and lower film surrounding plies are straight. Looking at an edge oriented transverse to the surrounding layers' fibre direction, the films have a certain waviness. The waviness results from the adaption of the films to the fibre bundles of the dry glass fibre fabrics during vacuum infusion. Due to the adaption to the

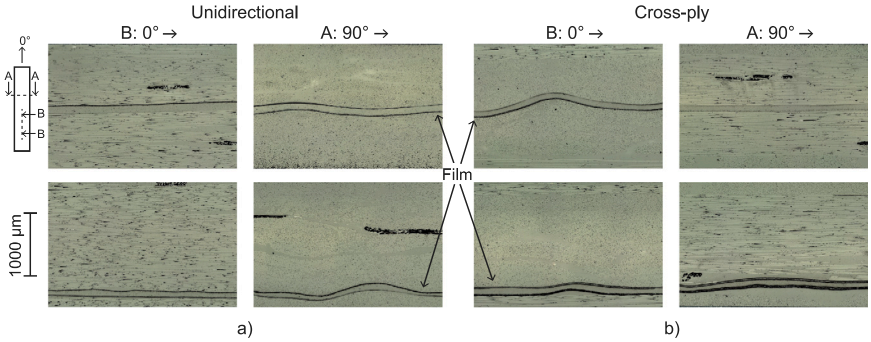

Fig. 2. Micrographs of (a) UD specimens (left: parallel to the 0° fibre direction, right: transverse to the 0° fibre direction, upper: film in the middle of the laminate, lower: film over the lower ply) and (b) CP specimens (left: parallel to the 0° fibre direction, right: transverse to the 0° fibre direction, upper: film in the middle of the laminate, lower: film over the lower layer).

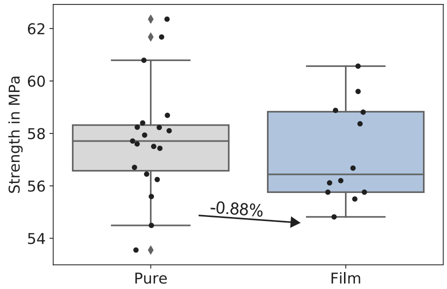

Fig. 3. Box plot including results of ILSS tests on neat GFRP and specimens with CNT film in the middle plane.

structure of the glass fabric, no resin rich regions are present directly at the films. The dark areas in the micrographs show the stitching yarns. During the discussion of the results, the influence of the waviness on the mechanical properties and sensing capabilities will be analysed.

3.2. ILSS tests

Fig. 3 shows a box plot of the ILSS of 19 neat GFRP specimens and 12 specimens with centrally integrated CNT/epoxy films. The ILSS of neat GFRP specimens and the GFRP specimens with integrated CNT films are similar. The standard deviations overlap and no significant difference is visible. The box plots show the median of the test values as horizontal lines, while the numbers show the decrease of the average value. Compared with neat GFRP, the average ILSS of the film specimens is marginally lower (−0.88%). The failure behaviour of all specimens does not reveal any delaminations directly at the CNT film. The delaminations occur cohesively, slightly above the film inside the GFRP, proofing a sufficient bonding between the pre-cured CNT/epoxy films and the surrounding matrix material. A curing of the films for 48 h at room temperature before integration, allows for easy, automated manufacturing on an industrial scale, as the films can easily be removed from the Teflon foil, cut to the desired shapes and placed on the dry glass fabrics.

3.3. Three-point bending tests

In three-point bending specimens, the films were placed under the top layer, in the middle of the laminate and over the bottom layer—theoretically resulting in three different local stress scenarios as schematically shown in Fig. 4. Placing the CNT sensors above the lowest layer results in a tensile and below the top layer in a compressive load inside the films. When perfectly integrating the films in the middle and therefore in the neutral axis, theoretically only shear is applied to the films and no volume change occurs.

The influence of the integrated films on strength and modulus in comparison with neat GFRP UD bending specimens is shown in the boxplot in Fig. 5. The horizontal lines resemble the medians, while the numbers describe the change of the average values. The average strength value decrease slightly for the UD specimens with films under the upper (−2.72%) and over the lower ply (−2.92%) while the average modulus values increase slightly (upper: 1.16%, lower: 1.11%). However, as the results of the specimen with films under the upper and over the lower ply lie within the standard deviation of the results for neat UD GFRP specimens, the slight changes are not significant. A significant increase of strength (+8.16%) and modulus (+13.27%) is visible for the UD bending specimens with films integrated in the middle plane. In this case, all 0°-plies are pushed further out relative to the centre plane of the laminate, leading to a higher bending stiffness. The trend is also visible for the upper and lower case, where the modulus is increase is smaller. In this case only one single 0°-ply is pushed further outwards leading to a small, not significant increase of the modulus.

Fig. 6 shows results of quasi-static three-point bending tests until failure and step-wise three-point bending tests for representative UD specimens with films under the upper ply, including stress and resistance change curves. The electrical resistance change ΔR in per cent is calculated according to Eq. (1) with the initial resistance R_0 and the current resistance R:

$$\Delta R = \frac{R - R_0}{R_0} \cdot 100. \tag{1}$$

The resistance change is negative throughout the entire bending test. At first, the resistance decrease has a lower slope and after the initial phase the slope increases. Shortly before the final failure, small steps in the resistance change are visible resembling steps in the stress curve due to failure of the first fibre bundles. The resistance change at final failure has an average value of $-2.72 \pm 0.31\%$. During step-wise tests, the same stress-anti-proportional resistance change is measurable with decreasing resistance during loading and increasing resistance during unloading. Up to 250 MPa, the resistance change is fully reversible during unloading. Afterwards, the irreversibility of the resistance change increases with higher stresses. When comparing the quasi-static and step-wise curves, it is evident that similar loads lead to similar resistance changes. Furthermore, the stresses leading to fully reversible resistance changes in step-wise tests are in the same range as the stresses before the slope transition towards the higher slope of the resistance change at the beginning of the quasi-static tests. The decreasing resistance is a consequence of the compressive loading state above the midplane of the laminate. The piezoresistive effect is known for CNT polymer composites and results from their heterogeneous structure as the compressive strain leads to a reduction of the tunnelling resistance or the formation of new conductive paths inside the CNT films as CNTs are moved closer together [6,44–46]. The irreversibility of the resistance change is caused by irreversible changes in the CNT network inside the films as not all of the formed

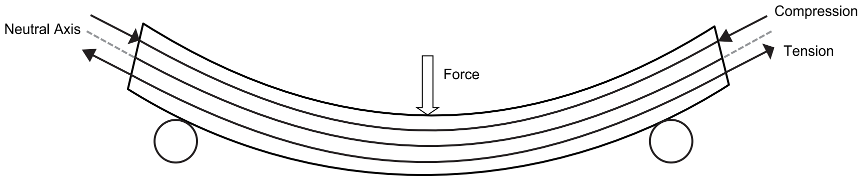

Fig. 4. Schematic representation of loading in three-point bending specimen—top film: compression, middle film: neutral axis, bottom film: tension.

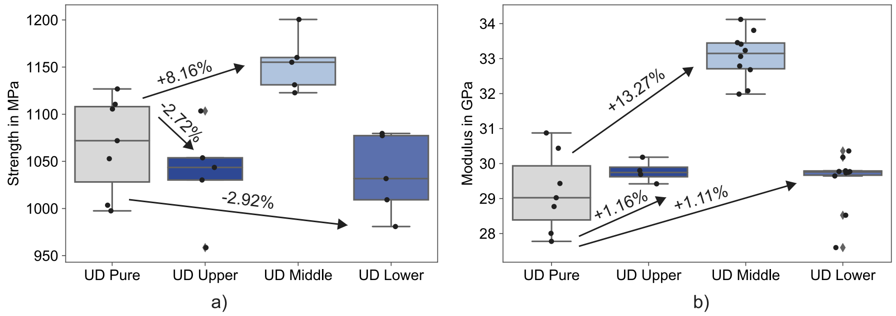

Fig. 5. Box plot including results of bending tests on UD neat GFRP and specimens with CNT film in different layers and per cent change of the average value—(a) strength, (b) modulus.

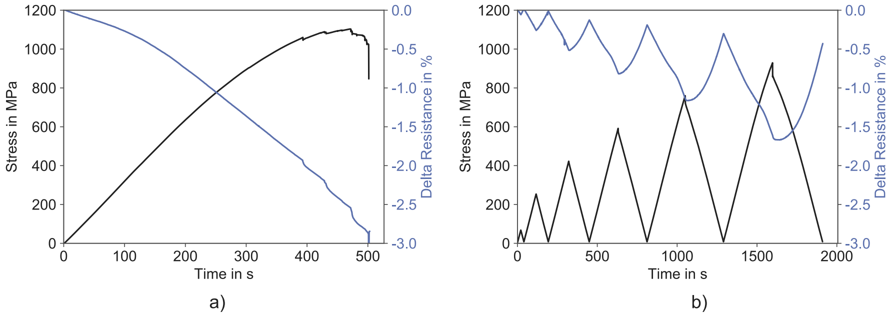

Fig. 6. Representative results of (a) quasi-static and (b) step-wise three-point bending tests on UD specimens with films under the upper ply including stress and resistance change.

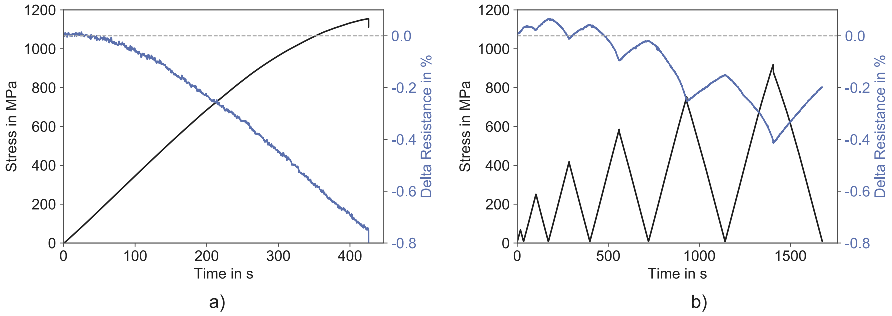

Fig. 7. Representative results of (a) quasi-static and (b) step-wise three-point bending tests on UD specimens with films in the middle including stress and resistance change.

paths are dissolved again. One reason might be the visible indention due to the upper roller that leads to local compression of the film. Overall, however, predicting the applied stress or strain is possible via the measured resistance change.

Representative results for UD bending specimens with films in the middle are presented in Fig. 7. In theory, the middle film lies in the neutral axis of the specimens, therefore only exposed to shear. In the ideal case, no volumetric change of the film is expected. Consequently, the influence on the CNT network and the resulting resistance change is expected to be minimal. The magnitude of the resistance change ($-0.73 \pm 0.14\%$) at final failure is indeed smaller than in the films under the upper and above the lower ply. However, a small resistance change is still measurable. The films have a certain thickness and due to the manufacturing process a small deviation to the neutral axis as well as a waviness transverse to the surrounding fibres' direction, as can be seen in the micrographs in Fig. 2. These effects lead to small resistance changes and influence the shape of the curve. The resistance change at the beginning of the quasi-static tests is very small. During the test, the slope becomes more negative resulting in a linear decrease. As visible in the representative resistance curve for the step-wise tests, a mixed positive and negative behaviour occurs during the test. The point at which the behaviour reverses is slightly different for all samples, but qualitatively the curves are similar. In terms of magnitude, the changes are very small, which makes the curves appear more jagged than for the upper and lower films. The mixed behaviour is likely caused by a change of tensile and compressive local stresses inside the film due to the slight deviation to the neutral axis. Possibly the waviness leads to specimens with parts of the film being slightly above and other bits being slightly below the neutral axis.

As depicted in Fig. 8, films integrated over the lower ply of UD bending specimens show a resistance increase during loading. The resistance increase is in very good agreement with the applied stress following all observable trends in the stress curve. As a consequence of the tensile strain, conductive paths within the films dissolve as CNTs move apart that were previously very close or in contact. This reduction of the conductive paths leads to a resistance increase. The measured resistance change at final failure has a magnitude of $2.31 \pm 0.17\%$, which has a similar absolute value as the resistance decrease measured in specimens with films under the upper ply. Step-wise tests show full reversibility of the resistance change up to 600 MPa. The reversible region corresponds with the linear region of the stress curve in the quasi-static tests. For unloading after exposure to higher stresses, the resistance change reaches a slightly negative value in the unloaded state at zero stress indicating more conductive paths inside the CNT film than at the beginning of the test. In summary of the UD bending tests, the low standard deviations in resistance change before final failure show that the manufacturing process of the integrated CNT film sensors is not only easy and automatable but also generates reproducible results even for specimens manufactured in different plates using several, separately produced films. In the bending tests on UD GFRP composites with films under the upper or over the lower ply, knowledge of the strength and resistance change at failure allows setting a threshold value that must not be exceeded to ensure a safe and reliable operation.

Similar tests have been performed on CP specimens. Median strength and modulus of the CP bending specimens increase for all configurations including CNT films compared to neat GFRP specimens, as shown by the horizontal lines in the box plot in Fig. 9. The standard deviations of the strength values overlap for all configurations. Nevertheless, the increase of the average values (depicted as numbers in the figure) is significant. An average strength increase of 4.72% is measured for the CP specimens with films under the upper layer. The lowest average strength increase (2.89%) is measured for the specimens with film in the middle, and the highest average strength increase of 9.46% for specimens with films integrated over the lower layer. The average modulus increase is more significant as there is almost no overlap of the standard deviations (8.25% for upper films, 7.24% for films in the middle and 4.58% for films integrated over the lower layer). The median value for lower films is higher than for middle films, but on the average this trend is the opposite.

The stress and resistance curves of representative CP specimens shown in Figs. 10–12 qualitatively show similar trends as the UD specimens. A local compressive strain inside the film under the upper layer leads to a negative resistance change. The average maximum resistance change before final failure is $-1.33 \pm 0.06\%$ an therefore approximately half of the measured resistance change in the UD bending specimens with films under the upper layer. The strength of the specimen is also approximately half of the UD specimens' strength. Full reversibility of the resistance change is given up to around 300 MPa, which resembles the entirely linear region of the quasi-static stress–time curve and the part of the resistance change curve with the initial slope. For higher stresses, some irreversible deformation is present in the specimens and films.

For CP specimens with the film in the middle, nearly no resistance change is measurable. The maximum resistance change is $0.12 \pm 0.04\%$. The noticeable noise in the measurement is a scaling effect and only appears because of the small scale. The resistance is increasing linearly until the stress curve flattens at around 300 MPa. Then, the resistance change starts to flatten and decreases. Similar behaviour is visible in the step-wise tests. At the beginning the resistance is increasing without clear evidence of the unloading. For higher stresses the steps become more pronounced and the maxima of the resistance change correspond to the maxima of the stress as for films with local tensile stress. The resistance change stays positive during unloading. Only during the final unloading the initial resistance is reached and at the end of the unloading the resistance is lower than in the beginning. As in the UD specimens, the change between increasing and decreasing trends can be attributed to changing local stresses inside the film due to deviations to the neutral axis.

Resistance change in films under the upper layer of CP specimens shows an excellent agreement with the stress. Step-wise tests reveal a nearly fully reversible resistance change up to the highest load step. Unlike in the UD samples, no change in resistance below zero is detectable when the CP specimens are fully unloaded. Therefore, a correlation between applied stress and measured resistance change is feasible. The waviness of the films in the lengthwise direction of the CP bending specimens does not have a noticeable influence on the resistance change.

In summary, the three-point bending tests on UD and CP specimens show that a localised strain monitoring inside GFRP structures is possible by inserting the CNT films in different positions. Local compressive (film under the upper layer) and tensile (film over the lower layer) stresses can be detected and monitored by negative and positive resistance changes using the piezoresistive effect of the CNT films. A correlation between stress or strain and resistance change is possible and reproducible for upper and lower films, as the comparison between different specimens as well as quasi-static and step-wise tests shows. Films in the middle layer, however, show small, mixed mode resistances change resulting from deviations to the neutral axis due to placement, thickness and waviness of the film. Due to the mixed mode nature, a certain resistance change cannot clearly be attributed to a specific stress. Mechanically, an integration of the film sensors in bending specimens has no significant or in many cases even a beneficial effect. The integrated films lead to a strength and modulus increase for all CP configurations and for UD specimens with middle films. Strength and modulus of UD specimens with upper and lower films do not show a significant change as they are within the standard deviation of the neat GFRP specimens.

3.4. Tensile tests

Fig. 13 shows box plots of tensile strength and modulus of UD neat GFRP specimens and specimens including CNT/epoxy films in the middle of the laminate. The average strength of the specimens is decreasing 7.79%, while the modulus is increasing 4.97%. The standard deviations slightly overlap for strength and modulus. The failure behaviour of failed neat UD GFRP specimens and specimens including films is similar. As structures often are designed concerning the modulus, the modulus increase can provide a positive design perspective under consideration of the strength decrease.

Fig. 14 presents the stress and resistance change curves of quasi-static and step-wise tensile tests on representative UD specimens. Mechanically, the specimens show a linear stress increase until brittle failure. The measured resistance change inside the UD specimens' films is positive and shows an excellent agreement with the stress up to failure. Similar to the local tensile stresses in bending, the applied strain under tensile load leads to higher distances of the CNTs. Consequently, the resistance increases as conductive paths within the films dissolve. The total resistance change is $5.71 \pm 0.65\%$. The step-wise tests reveal that the resistance change is fully reversible and follows the applied loading.

For CP specimens, the average tensile strength with integrated films decreases 1.89% compared to neat GFRP and the average modulus increases 4.74% (see Fig. 15). The standard deviation of the strength overlaps with the neat GFRP specimens' results. The average modulus increase lies within the standard deviation of the neat GFRP samples. Therefore, it can be concluded that the effect of the films on tensile strength and modulus of CP specimens is small and mostly neglectable. Tensile tests on CP specimens (representative results see Fig. 16) show

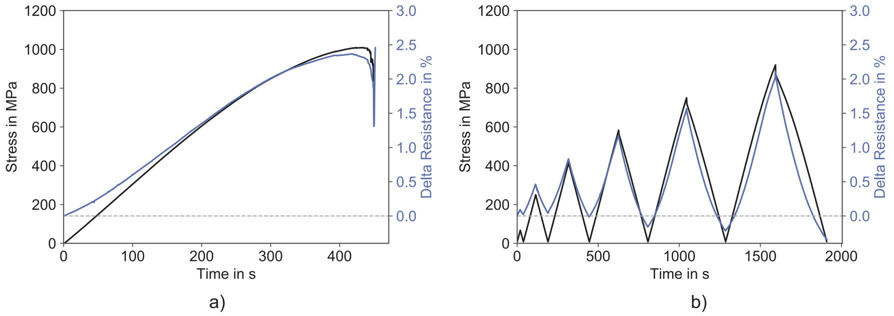

a)
b)

Fig. 8. Representative results of (a) quasi-static and (b) step-wise three-point bending tests on UD specimens with films over the lower ply including stress and resistance change.

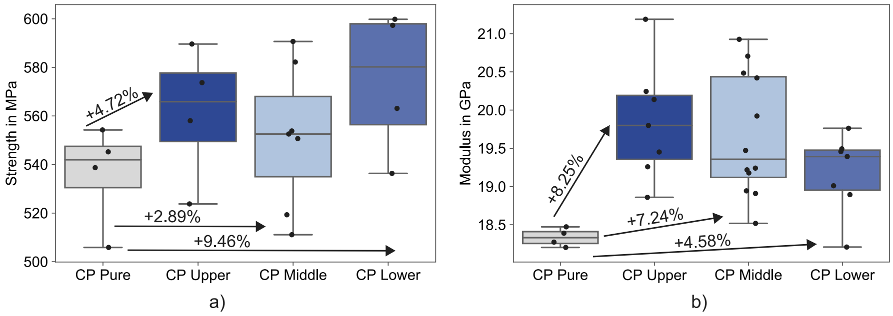

a)
b)

Fig. 9. Box plot including results of bending tests on CP neat GFRP and specimens with CNT film in different layers—(a) strength, (b) modulus.

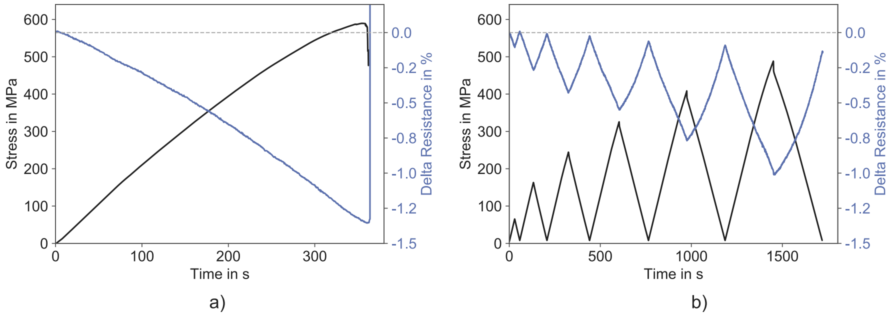

a)
b)

Fig. 10. Representative results of (a) quasi-static and (b) step-wise three-point bending tests on CP specimens with films under the upper layer including stress and resistance change.

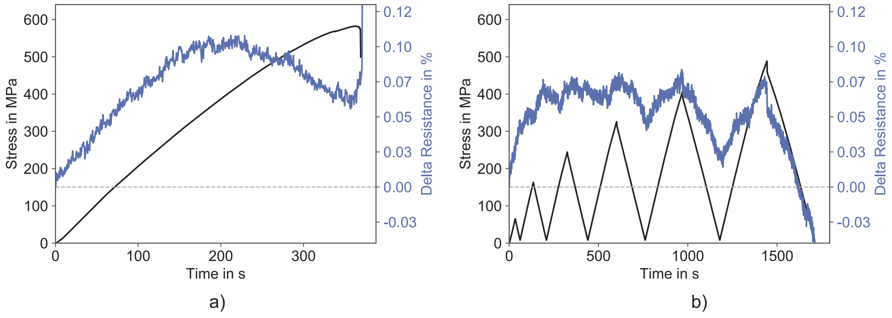

a)
b)

Fig. 11. Representative results of (a) quasi-static and (b) step-wise three-point bending tests on CP specimens with films in the middle including stress and resistance change.

a clear "knee" point in the stress curve with a stiffness decrease due to developing matrix cracks. The film stays intact until final failure and therefore the cracks are developing on both sides of the film as explained in further detail later. The crack spacing and failure behaviour of specimens with films and reference specimens are similar. Therefore, an in-situ crack counting in reference specimens can be seen as representative for development in film specimens. As visible in Fig. 17, the depicted curve of the counted cracks shows a steep increase around the "knee" point and slower crack development with higher strain. The resistance change shows a three-step behaviour (see Fig. 16). At first, there is a linear increase in resistance. The increase's slope is slightly smaller after the "knee" point. Towards the end, when the crack curve reaches saturation, a strong increase in resistance is visible. The resistance change at failure is 15.32 ± 3.9% and therefore approximately 2.7 times higher than for the UD specimens. However, the fracture strain of the specimens only shows a small deviation

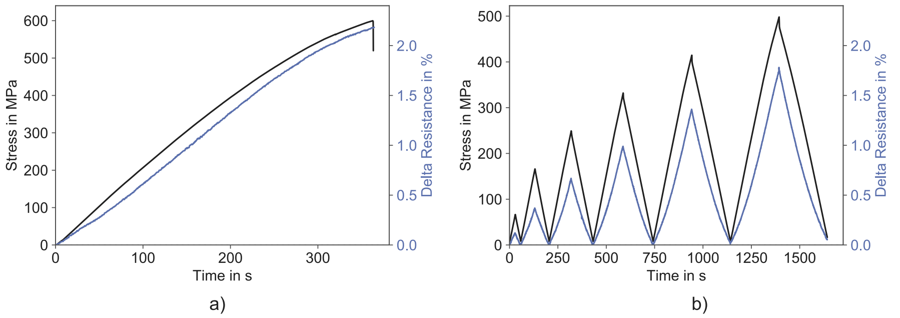

Fig. 12. Representative results of (a) quasi-static and (b) step-wise three-point bending tests on CP specimens with films over the lower layer including stress and resistance change.

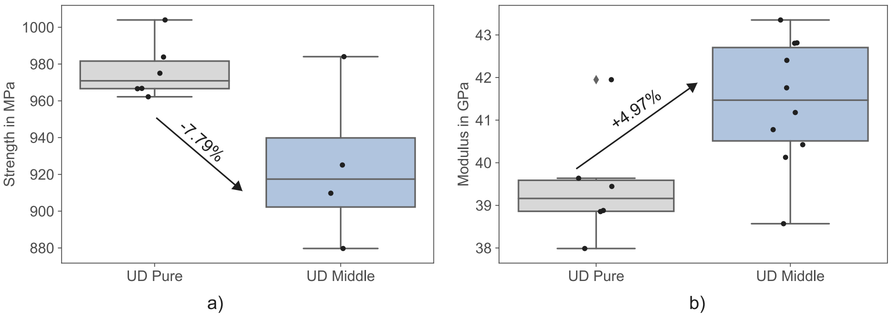

Fig. 13. Box plot including results of tensile tests on UD neat GFRP and specimens with CNT film in the middle plane—(a) strength, (b) modulus.

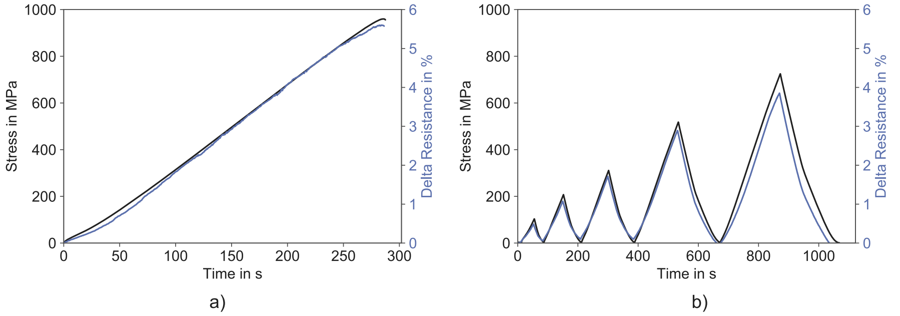

Fig. 14. Representative results of (a) quasi-static and (b) step-wise tensile tests on UD specimens including stress and resistance change.

between UD and CP specimens (UD: 2.35 ± 0.12, CP: 2.69 ± 0.03). The non-linear resistance increase in the CP specimens as opposed to the linear increase in the UD specimens is resulting from the different failure behaviour due to developing matrix cracks. In step-wise tests, the maxima and minima of the resistance change and stress correspond well, increasing stress leading to an increasing resistance change. The “knee” is visible in the stress as well as in the resistance change. However, during unloading, the resistance change is not fully reversible for the CP specimens, in contrast to the UD specimens, as cracks are not closing completely during unloading, which is explained in more detail using DIC images of the specimen edges. The DIC images in Figs. 18 and 19 show a high increase of local strain due to the cracks especially during crack opening towards the end of the tests. The film is located in the middle, parallel to the long edge of the image. The cracks form on both sides of the CNT film and do not span the whole thickness of the specimens. During higher rate of crack formation, the local strains are smaller. With fewer cracks developing, the increasing stress leads to an opening of the existing cracks and the local strains at the film increase in intensity, amount, and area. Therefore, the high resistance increase towards the end of the tensile tests on CP specimens can be attributed to high local strains in the CNT film due to crack opening. DIC of step-wise tests shows the crack development at lower stresses. At the maximum of step one, the visible section includes two cracks. During unloading, the cracks close but some local strain remains in the cracked areas, visible as slightly turquoise areas. For comparison the scale is the same for all images. With a re-scaling, however, the remaining strain would become more visible. The remaining strain after the first load step is small compared with the remaining strains for further unloadings. The irreversibility of the resistance change during unloading results from the remaining local strains in the films and is influenced by the value of the remaining strain. New cracks form during the second loading step. Although some new cracks are still formed in the specimen for higher stresses as the crack development in Fig. 17 shows, within the depicted area, mostly the existing cracks open and the local strains increase for higher stresses. A new crack develops during the fourth loading step. During the high rise of the resistance towards the end of the test, the crack opening and, therefore, the local strains drastically increase in many cracks. Results of the CP tensile tests show the films’ ability to monitor local strain increases inside the specimens due to the cracks. The crack opening towards the end of the tensile test results in a drastic resistance increase. Therefore, a localised SHM via resistance measurements is possible. Threshold values of the resistance change can be set for UD and CP specimens to avoid a final failure of the material.

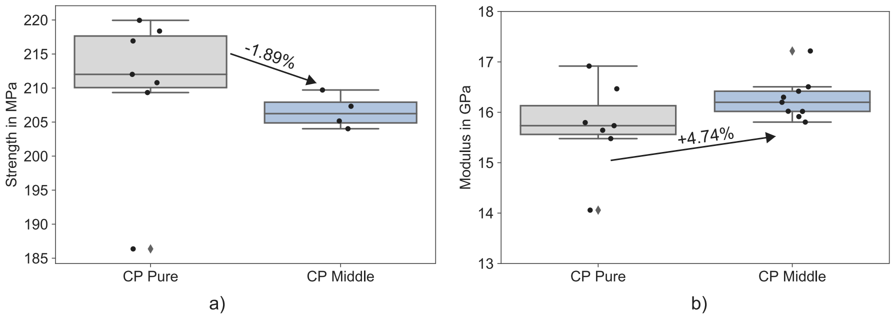

Fig. 15. Box plot including results of tensile tests on CP neat GFRP and specimens with CNT film in the middle plane—(a) strength, (b) modulus.

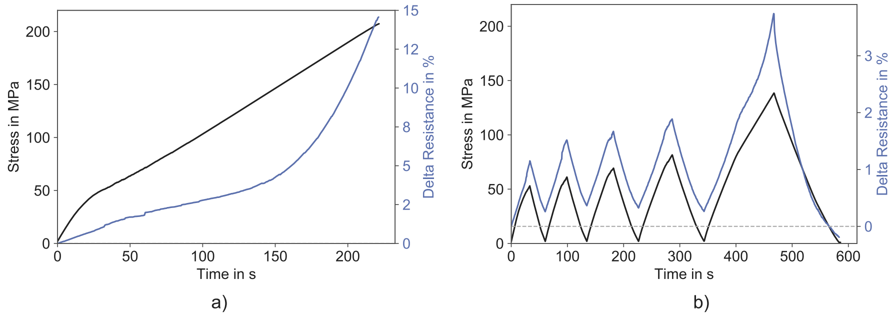

Fig. 16. Representative results of (a) quasi-static and (b) step-wise tensile tests on CP specimens including stress and resistance change.

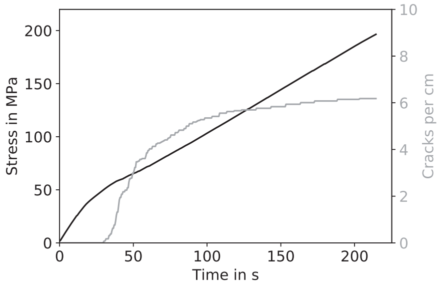

Fig. 17. Crack development in CP reference specimen without films.

3.4.1. *Open hole tensile tests*

As the tensile tests on CP specimens revealed the ability to monitor local strain peaks inside GFRP, the films are inserted around the holes in OHT specimens. An SHM of the vicinity of holes is desired, especially in large structures, as the stress concentrations around holes promote early failure. Fig. 20 shows the results of representative OHT specimens for each of the three tested configurations (films between the ±45°-layer and the 90°-layer, between the 90°-layer and the 0°-layer and in the middle of the laminate between the 0°-plies) including stress and resistance change curves for film around the hole and in the near field.

All stress–time curves have a linear behaviour until sudden, brittle failure. The resistance change curves are different for the three configurations. However, for all configurations, the films at the hole exhibit a higher resistance change than the films in the near field. For films in

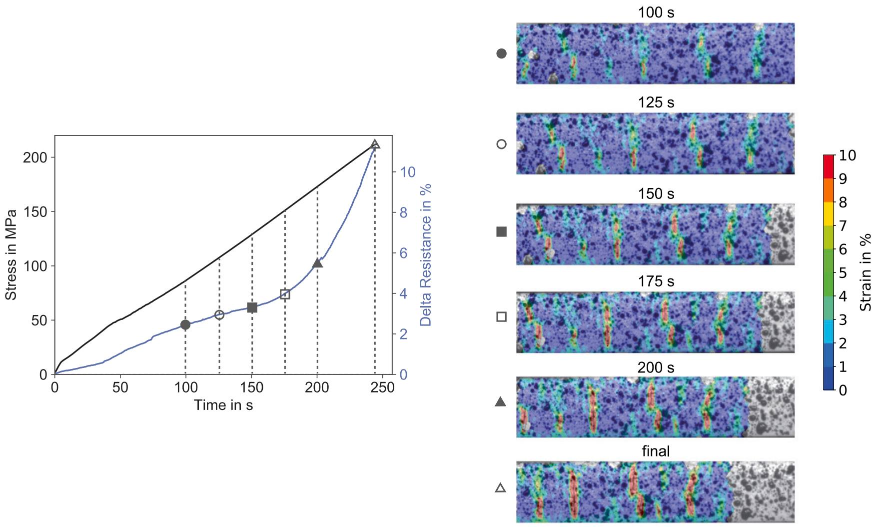

Fig. 18. Results of a quasi-static tensile test on a cross-ply specimen and corresponding digital image correlation pictures for six specific time-steps.

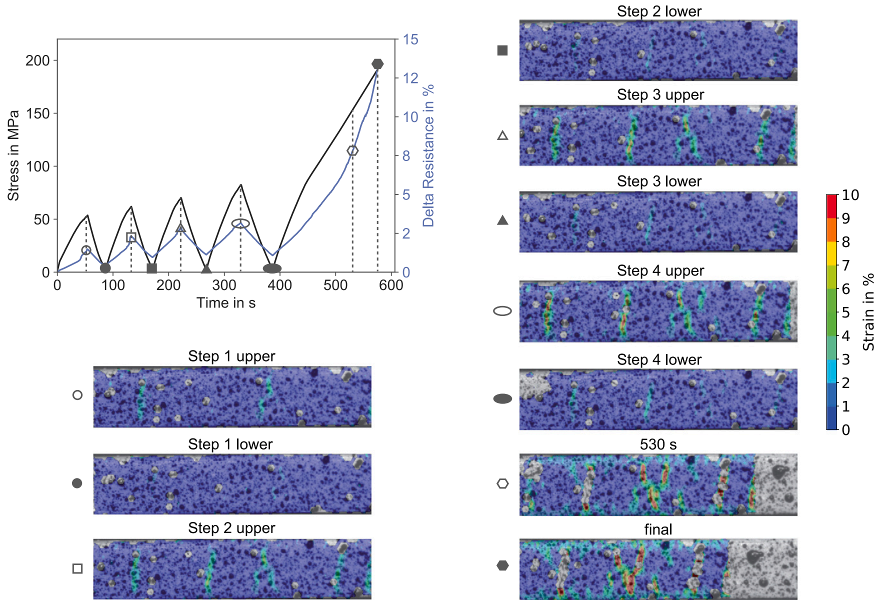

Fig. 19. Results of a step-wise tensile test on a cross-ply specimen and corresponding digital image correlation pictures for ten specific time-steps.

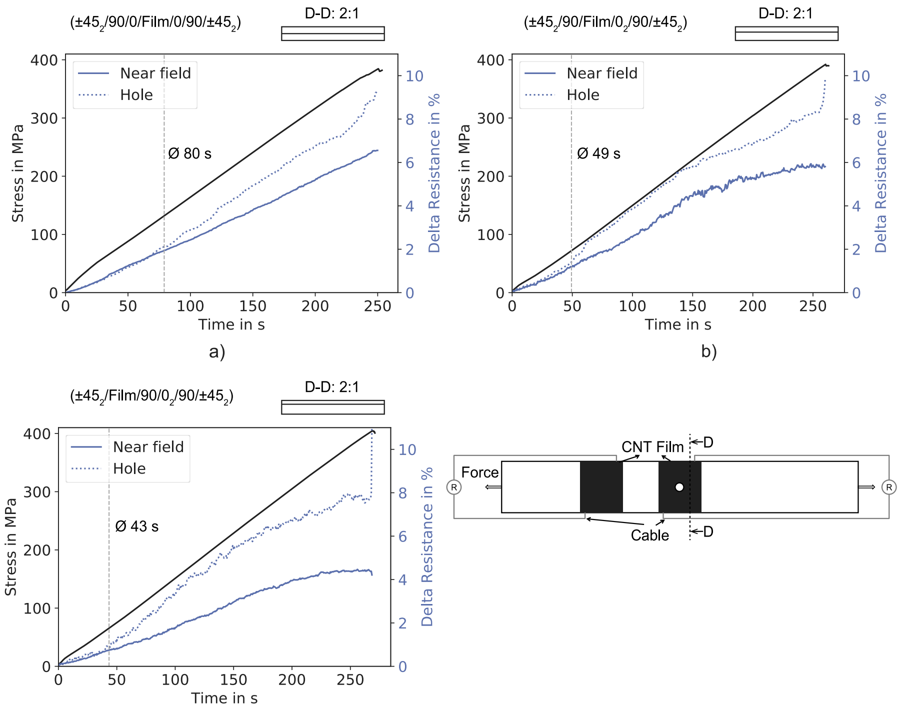

a)

b)

c)

d)

Fig. 20. Representative results of OHT tests on quasi-isotropic GFRP with CNT films in different layers—(a) between 0°-plies in the middle of the laminate, (b) between the 90°-layer and the 0°-layer, (c) between the ±45°-layer and the 90°-layer. Resistance change is shown for the film in the vicinity of the hole and in the near field.

the middle of the laminate between the 0°-plies the resistance change of the film in the near field is linear until final failure and reaches a maximum value of $6.11 \pm 0.38\%$. Qualitatively, the course of the change in resistance is thus similar to tensile tests on UD specimens. At the beginning of the test, the change in resistance of the film at the hole is equal to that of the film in the near field. In all samples with film between the 0°-plies, the resistance change in the film at the hole is bigger than in the near field film from an average of 80 s onwards, which is also marked with the dashed line in the diagram (Fig. 20). After that, the resistance change of the films at the hole has a higher slope but still a mostly linear shape. Shortly before failure, a stronger increase of the resistance change at the hole is measured. The absolute value of final resistance change at the hole varies between the specimens as the strain in the film is influenced by the damage state around the hole. For films located between the 90°-layer and the 0°-layer, the resistance change in the near field is linear only at the beginning and then flattens out noticeably. The absolute maximum resistance change for the near field films is similar to that with films between the 0°-plies. However, the difference between hole and near field films' resistance changes is visible much earlier than for films between the 0°-plies. On average, the film at the hole shows the bigger resistance change compared to the near field already after 49 s as shown with the dashed line in Fig. 20.

Although the resistance change is bigger, the shape of the resistance change at the hole is qualitatively similar to that of the near field and shows the same flattening. In specimens with films between the ±45°-layer and the 90°-layer the deviation between resistance at the hole and in the near field is starting at 43 s (dashed line in Fig. 20) and shows the highest deviation of all configurations. The resistance change in the near field qualitatively has a similar shape as the near field films integrated between 90°-layer and the 0°-layer, but the maximum value is lower. The deviation between near field resistance change and resistance change at the hole is attributed to local strains around the hole. The flattening of the resistance change curve (in the case of films between the ±45°-layer and the 90°-layer and ±90°-layer and the 0°-layer) shows a decrease of local strain due to local damage, e.g., in the form of delaminations. Therefore, the CNT strain sensors are able to monitor local strains around the hole in different layers, revealing valuable insights into the failure process. A prediction of failure using threshold resistance change values is possible. A change of the film's shape, e.g., to a triangle resembling the highly loaded areas even better, might increase the sensitivity.

4. Conclusion

The integrated SWCNT/epoxy films, presented within this paper's scope, are able to monitor strains inside GFRP for different load cases and lay-ups over large material sections or selectively in highly loaded areas, mostly with no significant or even positive effects on the mechanical properties. Therefore, the strain measurements on integrated CNT films offer significant advantages compared to classic surface-mounted strain gauges. The CNT-films' piezoresistive effect, enables correlation of stress or strain and resistance change. Local compressive stresses lead to a resistance decrease which is anti-proportional to the applied stress. In contrast, tensile stresses induce a stress-proportional increase in resistance. During unloading, damages as matrix cracks that result in remaining local strains, result in irreversible resistance changes. Drastic resistance increases after crack saturation in CP tensile specimens can be attributed to high local strains due to crack opening, as DIC images reveal. Knowledge of the effects and an integration of the films in specific layers or locations offers a high design flexibility and provides the means for localised strain and damage monitoring. OHT tests showed the ability to monitor local strains in highly loaded areas and at different material depths, gaining valuable insights into the failure process, including local delaminations. Higher strains around the hole can reliably be monitored. The correlation between resistance change and strain and the knowledge of the effects of certain damages on the resistance change offers the possibility to detect critical loads and to define a resistance threshold shortly before final failure. The CNT films allow for a tailored SHM in GFRP with low manufacturing and installation effort as the method of embedding pre-cured CNT/epoxy films offers an easy and automatable way of manufacturing that can be performed on an industrial scale. Furthermore, localised monitoring of CFRP structures may be enabled when embedding the CNT films between isolating epoxy layers.

Declaration of competing interest

The authors declare that they have no known competing financial interests or personal relationships that could have appeared to influence the work reported in this paper.

Funding

This research was funded by the Deutsche Forschungsgemeinschaft (DFG - German Research Foundation) within the project number 393868053. We acknowledge support for the Open Access fees by Hamburg University of Technology (TUHH) in the funding programme Open Access Publishing.

References

[1] K. Diamanti, C. Soutis, Structural health monitoring techniques for aircraft composite structures, Prog. Aerosp. Sci. 46 (8) (2010) 342–352, http://dx.doi.org/10.1016/j.paerosci.2010.05.001.

[2] J. Cai, L. Qiu, S. Yuan, L. Shi, P. Liu, D. Liang, Structural health monitoring for composite materials, in: N. Hu (Ed.), Composites and their Applications, InTech, 2012, http://dx.doi.org/10.5772/48215.

[3] V. Giurgiutiu, Structural Health Monitoring of Aerospace Composites, Academic Press an imprint of Elsevier, Amsterdam and Boston and Heidelberg, 2016.

[4] K. Schulte, C. Baron, Load and failure analyses of CFRP laminates by means of electrical resistivity measurements, Compos. Sci. Technol. 36 (1) (1989) 63–76, http://dx.doi.org/10.1016/0266-3538(89)90016-X.

[5] M. Kupke, K. Schulte, R. Schüler, Non-destructive testing of FRP by d.c. and a.c. electrical methods, Compos. Sci. Technol. 61 (6) (2001) 837–847, http://dx.doi.org/10.1016/S0266-3538(00)00180-9.

[6] F. Carmona, R. Canet, P. Delhaes, Piezoresistivity of heterogeneous solids, J. Appl. Phys. 61 (7) (1987) 2550–2557, http://dx.doi.org/10.1063/1.337932.

[7] H. Zhang, E. Bilotti, T. Peijs, The use of carbon nanotubes for damage sensing and structural health monitoring in laminated composites: a review, Nanocomposites 1 (4) (2015) 167–184, http://dx.doi.org/10.1080/20550324.2015.1113639.

[8] T. Xiao, C. Qian, R. Yin, K. Wang, Y. Gao, F. Xuan, 3D printing of flexible strain sensor array based on UV–Curable multiwalled carbon nanotube/elastomer composite, Adv. Mater. Technol. 6 (1) (2021) 2000745, http://dx.doi.org/10.1002/admt.202000745.

[9] Z.-H. Tang, Y.-Q. Li, P. Huang, H. Wang, N. Hu, S.-Y. Fu, Comprehensive evaluation of the piezoresistive behavior of carbon nanotube-based composite strain sensors, Compos. Sci. Technol. 208 (2021) 108761, http://dx.doi.org/10.1016/j.compscitech.2021.108761.

[10] M. Kupke, H.-P. Wentzel, K. Schulte, Electrically conductive glass fibre reinforced epoxy resin, Mater. Res. Innov. 2 (3) (1998) 164–169, http://dx.doi.org/10.1007/s100190050079.

[11] E.T. Thostenson, T.-W. Chou, Carbon nanotube networks: Sensing of distributed strain and damage for life prediction and self healing, Adv. Mater. 18 (21) (2006) 2837–2841, http://dx.doi.org/10.1002/adma.200600977.

[12] L. Böger, M.H.G. Wichmann, L.O. Meyer, K. Schulte, Load and health monitoring in glass fibre reinforced composites with an electrically conductive nanocomposite epoxy matrix, Compos. Sci. Technol. 68 (7) (2008) 1886–1894, http://dx.doi.org/10.1016/j.compscitech.2008.01.001.

[13] L. Gao, E.T. Thostenson, Z. Zhang, T.-W. Chou, Sensing of damage mechanisms in fiber-reinforced composites under cyclic loading using carbon nanotubes, Adv. Funct. Mater. 19 (1) (2009) 123–130, http://dx.doi.org/10.1002/adfm.200800865.

[14] L. Gao, E.T. Thostenson, Z. Zhang, J.-H. Byun, T.-W. Chou, Damage monitoring in fiber-reinforced composites under fatigue loading using carbon nanotube networks, Phil. Mag. 90 (31–32) (2010) 4085–4099, http://dx.doi.org/10.1080/14786430903352649.

[15] S. Wu, R.B. Ladani, A.R. Ravindran, J. Zhang, A.P. Mouritz, A.J. Kinloch, C.H. Wang, Aligning carbon nanofibres in glass-fibre/epoxy composites to improve interlaminar toughness and crack-detection capability, Compos. Sci. Technol. 152 (2017) 46–56, http://dx.doi.org/10.1016/j.compscitech.2017.09.007.

[16] P. Dharap, Z. Li, S. Nagarajaiah, E.V. Barrera, Nanotube film based on single-wall carbon nanotubes for strain sensing, Nanotechnology 15 (3) (2004) 379–382, http://dx.doi.org/10.1088/0957-4484/15/3/026.

[17] P. Dharap, Z. Li, S. Nagarajaiah, E.V. Barrera, Flexural strain sensing using carbon nanotube film, Sensor Rev. 24 (3) (2004) 271–273, http://dx.doi.org/10.1108/02602280410545399.

[18] I. Kang, M.J. Schulz, J.H. Kim, V. Shanov, D. Shi, A carbon nanotube strain sensor for structural health monitoring, Smart Mater. Struct. 15 (3) (2006) 737–748, http://dx.doi.org/10.1088/0964-1726/15/3/009.

[19] B.R. Loyola, V. La Saponara, K.J. Loh, In situ strain monitoring of fiber-reinforced polymers using embedded piezoresistive nanocomposites, J. Mater. Sci. 45 (24) (2010) 6786–6798, http://dx.doi.org/10.1007/s10853-010-4775-y.

[20] B.R. Loyola, K.J. Loh, V. La Saponara, Static and dynamic strain monitoring of GFRP composites using carbon nanotube thin films, in: M. Tomizuka (Ed.), Sensors and Smart Structures Technologies for Civil, Mechanical, and Aerospace Systems 2011, in: SPIE Proceedings, SPIE, 2011, 798108, http://dx.doi.org/10.1117/12.881006.

[21] B.M. Lee, S. Gupta, K.J. Loh, S. Nagarajaiah, Strain sensing and structural health monitoring using nanofilms and nanocomposites, in: K.J. Loh, S. Nagarajaiah (Eds.), Innovative Developments of Advanced Multifunctional Nanocomposites in Civil and Structural Engineering, in: Woodhead Publishing Series in Civil and Structural Engineering, Elsevier Woodhead Publishing, Duxford, UK, 2016, pp. 303–326, http://dx.doi.org/10.1016/B978-1-78242-326-3.00013-0.

[22] D. Zymelka, K. Togashi, T. Kobayashi, Carbon-based printed strain sensor array for remote and automated structural health monitoring, Smart Mater. Struct. 29 (10) (2020) 105022, http://dx.doi.org/10.1088/1361-665x/aba81c.

[23] N.D. Alexopoulos, C. Bartholome, P. Poulin, Z. Marioli-Riga, Structural health monitoring of glass fiber reinforced composites using embedded carbon nanotube (CNT) fibers, Compos. Sci. Technol. 70 (2) (2010) 260–271, http://dx.doi.org/10.1016/j.compscitech.2009.10.017.

[24] N. Wiegand, E. Mäder, Multifunctional interphases: Percolation behavior, interphase modification, and electro-mechanical response of carbon nanotubes in glass fiber polypropylene composites, Adv. Energy Mater. 18 (3) (2016) 376–384, http://dx.doi.org/10.1002/adem.201500447.

[25] M.T. Müller, H.F. Pötzsch, U. Gohs, G. Heinrich, Online structural-health monitoring of glass fiber-reinforced thermoplastics using different carbon allotropes in the interphase, Materials (Basel, Switzerland) 11 (7) (2018) http://dx.doi.org/10.3390/ma11071075.

[26] J. Sebastian, N. Schehl, M. Bouchard, M. Boehle, L. Li, A. Lagounov, K. Lafdi, Health monitoring of structural composites with embedded carbon nanotube coated glass fiber sensors, Carbon 66 (3) (2014) 191–200, http://dx.doi.org/10.1016/j.carbon.2013.08.058.

[27] S.-L. Gao, R.-C. Zhuang, J. Zhang, J.-W. Liu, E. Mäder, Glass fibers with carbon nanotube networks as multifunctional sensors, Adv. Funct. Mater. 20 (12) (2010) 1885–1893, http://dx.doi.org/10.1002/adfm.201000283.

[28] H. Zhang, M. Kuwata, E. Bilotti, T. Peijs, N.M. Huang, Integrated damage sensing in fibre-reinforced composites with extremely low carbon nanotube loadings, J. Nanomater. 2015 (2015) 785834, http://dx.doi.org/10.1155/2015/785834.

[29] S. Nag-Chowdhury, H. Bellegou, I. Pillin, M. Castro, P. Longrais, J.F. Feller, Non-intrusive health monitoring of infused composites with embedded carbon quantum piezo-resistive sensors, Compos. Sci. Technol. 123 (2016) 286–294, http://dx.doi.org/10.1016/j.compscitech.2016.01.004.

[30] J.A. Rodríguez-González, C. Rubio-González, J.A. Soto-Cajiga, Piezoresistive response of spray-coated multiwalled carbon nanotube/glass fiber/epoxy composites under flexural loading, Fibers Polym. 20 (8) (2019) 1673–1683, http://dx.doi.org/10.1007/s12221-019-8711-8.

[31] Y.-T. Jung, H.D. Roh, I.-Y. Lee, Y.-B. Park, Strain sensing and progressive failure monitoring of glass-fiber-reinforced composites using percolated carbon nanotube networks, Funct. Compos. Struct. 2 (1) (2020) 015006, http://dx.doi.org/10.1088/2631-6331/ab7bc4.

[32] K. Aly, A. Li, P.D. Bradford, Strain sensing in composites using aligned carbon nanotube sheets embedded in the interlaminar region, Composites A 90 (2016) 536–548, http://dx.doi.org/10.1016/j.compositesa.2016.08.003.

[33] K. Aly, A. Li, P.D. Bradford, In-situ monitoring of woven glass fiber reinforced composites under flexural loading through embedded aligned carbon nanotube sheets, J. Compos. Mater. 52 (20) (2018) 2777–2788, http://dx.doi.org/10.1177/0021998317754128.

[34] O.G. Kravchenko, D. Pedrazzoli, D. Kovtun, X. Qian, I. Manas-Zloczower, Incorporation of plasma-functionalized carbon nanostructures in composite laminates for interlaminar reinforcement and delamination crack monitoring, J. Phys. Chem. Solids 112 (2018) 163–170, http://dx.doi.org/10.1016/j.jpcs.2017.09.018.

[35] O.G. Kravchenko, D. Pedrazzoli, V.S. Bonab, I. Manas-Zloczower, Conductive interlaminar interfaces for structural health monitoring in composite laminates under fatigue loading, Mater. Des. 160 (7) (2018) 1217–1225, http://dx.doi.org/10.1016/j.matdes.2018.10.045.

[36] A.S. Wu, W.-J. Na, W.-R. Yu, J.-H. Byun, T.-W. Chou, Carbon nanotube film interlayer for strain and damage sensing in composites during dynamic compressive loading, Appl. Phys. Lett. 101 (22) (2012) 221909, http://dx.doi.org/10.1063/1.4765654.

[37] P. Slobodian, S. Lloret Pertegás, P. Riha, J. Matyas, R. Olejnik, R. Schledjewski, M. Kovar, Glass fiber/epoxy composites with integrated layer of carbon nanotubes for deformation detection, Compos. Sci. Technol. 156 (2018) 61–69, http://dx.doi.org/10.1016/j.compscitech.2017.12.012.

[38] H. Meeuw, J. Körbelin, D. von Bernstorff, T. Augustin, W.V. Liebig, B. Fiedler, Smart dispersion: Validation of OCT and impedance spectroscopy as solutions for in-situ dispersion analysis of CNP/EP-composites, Materialia 1 (9) (2018) 185–197, http://dx.doi.org/10.1016/j.mtla.2018.06.002.

[39] H. Meeuw, V.K. Wisniewski, U. Köpke, A.S. Nia, A.R. Vázquez, M.R. Lohe, X. Feng, B. Fiedler, In-line monitoring of carbon nanoparticle epoxy dispersion processes, Prod. Eng. 13 (3–4) (2019) 373–390, http://dx.doi.org/10.1007/s11740-019-00884-5.

[40] ASTM D2344 / D2344M-16, Test Method for Short-Beam Strength of Polymer Matrix Composite Materials and Their Laminates, ASTM International, West Conshohocken, PA, 2016, http://dx.doi.org/10.1520/D2344_D2344M-16.

[41] DINENISO 14125, Fibre-reinforced plastic composites - determination of flexural properties, 2011.

[42] DINENISO 527-4, Plastics - Determination of tensile properties - Part 4: Test conditions for isotropic and anisotropic fibre-reinforced plastic composites, 1997.

[43] ASTM D5766/ D5766M-11, Test Method for Open-Hole Tensile Strength of Polymer Matrix Composite Laminates, ASTM International, West Conshohocken, PA, 2018, http://dx.doi.org/10.1520/D5766_D5766M-11R18.

[44] N. Hu, Y. Karube, C. Yan, Z. Masuda, H. Fukunaga, Tunneling effect in a polymer/carbon nanotube nanocomposite strain sensor, Acta Mater. 56 (13) (2008) 2929–2936, http://dx.doi.org/10.1016/j.actamat.2008.02.030.

[45] M.H.G. Wichmann, S.T. Buschhorn, J. Gehrmann, K. Schulte, Piezoresistive response of epoxy composites with carbon nanoparticles under tensile load, Phys. Rev. B 80 (24) (2009) 667, http://dx.doi.org/10.1103/PhysRevB.80.245437.

[46] H. Meeuw, C. Viets, W.V. Liebig, K. Schulte, B. Fiedler, Morphological influence of carbon nanofillers on the piezoresistive response of carbon nanoparticle/epoxy composites under mechanical load, Eur. Polym. J. 85 (21) (2016) 198–210, http://dx.doi.org/10.1016/j.eurpolymj.2016.10.027.